Science Advances
AAAS

advances.sciencemag.org/cgi/content/full/6/7/eaay8065/DC1

Supplementary Materials for

Thermoelectric properties of a semicrystalline polymer doped beyond the insulator-to-metal transition by electrolyte gating

Hisaaki Tanaka*, Kaito Kanahashi, Naoya Takekoshi, Hiroaki Mada, Hiroshi Ito*, Yukihiro Shimoi,
Hiromichi Ohta, Taishi Takenobu*

*Corresponding author. Email: htanaka@nuap.nagoya-u.ac.jp (H.T.); ito@nuap.nagoya-u.ac.jp (H.I.);
takenobu@nagoya-u.jp (T.T.)

Published 14 February 2020, *Sci. Adv.* **6**, eaay8065 (2020)
DOI: 10.1126/sciadv.aay8065

This PDF file includes:

Section S1. *S*-σ relations expected for conventional semiconductors and metals

In conventional non-degenerate semiconductors, the Seebeck coefficient is formulated as

$$S = \frac{k_{\mathrm{B}}}{e}\left(\frac{E_{\mathrm{c}}-E_F}{k_{\mathrm{B}}T} + \mathrm{const.}\right) \tag{1}$$

where E_{F} is the Fermi energy level, E_{c} is the energy at the conduction band edge, k_{B} is Boltzmann constant, and e is the elementary charge (*22, 49*). This equation predicts a logarithmic relation of $S \propto \ln(n)$ with respect to the thermally activated carrier concentration n, and then the S-σ relation of $S \propto \ln(\sigma)$ is derived under the condition of constant mobility. For the degenerate or metallic electronic states, the Seebeck coefficient is described by the Mott equation

$$S = \frac{\pi^2}{3e} k_B^2 T \frac{\partial \ln[\sigma(E)]}{\partial E}\Big|_{E=E_{\mathrm{F}}} \tag{2}$$

where E_{F} is the Fermi energy and $\sigma(E)$ is the energy-dependent conductivity function (*22, 26*). This equation expects the relation of $S \propto 1/\sigma^{-1}$ under the condition of $[\partial\sigma(E)/\partial E =$ const.]. Clearly, the power factor in this case is a decreasing function of the electrical conductivity.

Section S2. Effects of high V_{g} on the transport and thermoelectric properties

Since the electrolyte-gating technique utilizes an electrochemical process for doping, the application of a high V_{g} can cause unintentional side reactions, resulting in the degradation of the TFT device. Although we limited the V_{g} value to be sufficiently lower than the electrochemical window of [DEME][TFSI] in the present study, we examined the change in the thermoelectric properties induced by applying relatively high $|V_{\mathrm{g}}|$ values to avoid any unintentional effects such as overdoping, which can suppress the conductivity (*10*). Fig. S1A shows the S-σ relation obtained by applying high V_{g} values. The inset shows the

V_g dependence of σ (transfer characteristics) obtained for the same device. We clearly observe that σ exhibits a peak at a certain V_g value and starts to decrease as $|V_g|$ increases. This behaviour is often observed in electrolyte-gated polymer transistors (*50*-*52*). In this case, we observe that both the transfer characteristics and the S-σ relation become irreversible; i.e., the upward and downward V_g scans do not coincide with each other, implying that some irreversible degradation is induced in the device.

However, when we limit $|V_g|$ to be less than the value where the maximum σ is observed in the transfer characteristics, the S-σ relation is highly reversible, as shown in Fig. S1B, although the transfer characteristics exhibit considerable hysteresis due to the slow time scale of the present electrochemical processes, as shown in the inset. This result clearly indicates that the irreversible degradation of the device can be avoided if V_g is kept sufficiently lower than the critical value where σ shows a peak. However, owing to the sample dependence of the threshold voltage, the critical V_g cannot be specified to a single value throughout the present study. In the case of the thermoelectric properties in Fig. 1E, $|V_g|$ is kept below 1.9 V. We typically limit our discussion to the range of $S > 10$ μV/K in the present experiments.

We note here that the measurements shown in Fig. S1B are performed on the PBTTT (with tetradecyl side chains) thin film fabricated by the flow-coating method followed by annealing at 250 °C to form the ribbon phase (*53*). The shape of the S-σ relation is almost unaffected by the change in alkyl chain length or the fabrication method of the thin film.

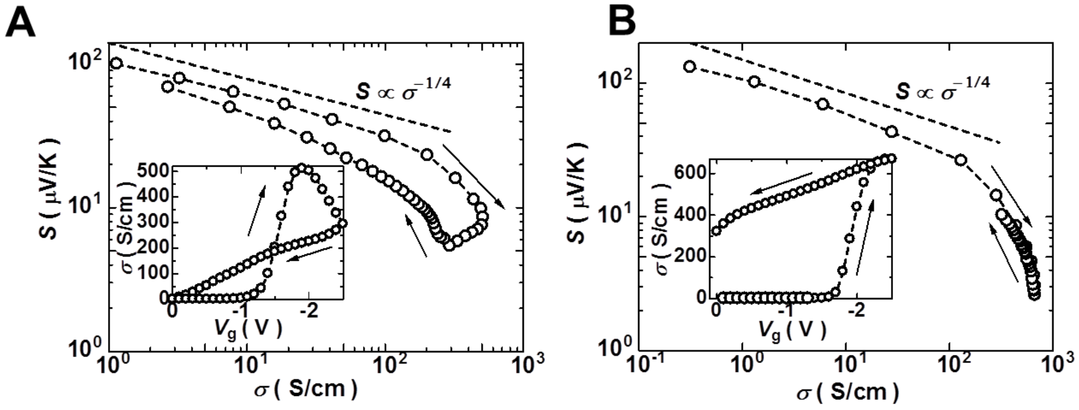

Fig. S1. Thermoelectric properties of the electrolyte-gated PBTTT thin films. (**A**) The S-σ relation measured beyond the critical V_g value, where the maximum σ is observed in the transfer characteristics, as shown in the inset, and (**B**) the S-σ relation measured by limiting $|V_g|$ below the critical value.

Section S3. In situ GIXD measurements during the application of V_g

In addition to the ex situ GIXD measurements shown in Fig. 2, we also tried to obtain diffraction data during the application of V_g to the electrolyte-gated TFT device. In this case, the gate insulator on top of the polymer film significantly affects the diffraction data. To minimize this effect, we adopt a thin ion-gel insulator with a thickness of ~1 μm. We could not observe the in-plane (010) peak corresponding to π–π stacking, presumably due to its low intensity, which can cause the peak to be easily masked by the background from the substrate and/or ion-gel film; however, a clear $|V_g|$ dependence of the out-of-plane (100) peak position is observed, as shown in Fig.S2A. In this experiment, we examined both upward and downward $|V_g|$ scans to confirm the reversibility of the doping-induced structural changes. We observe a similar shift in the (100) peak towards the lower q_z values as $|V_g|$ increases, as in the ex situ measurements in Fig. 2B, indicating lattice expansion due to anion intercalation. This process takes place almost reversibly with respect to the change of the V_g value.

Here, we repeated the measurements twice at each V_g with the time interval of 20 minutes to confirm the time response of the doping/dedoping process. We observe a clear difference of the peak position between these two measurements, indicating that the time response of the doping/dedoping process takes more than 20 minutes. This slow response is consistent with the large hysteresis observed in Fig. S2B. However, we notice that the lattice expansion in the out-of-plane direction almost saturates to be ~7 Å as shown in Fig. S2B. This value, which is even larger than that observed in the ex situ measurements, is very close to the size of the TFSI anion of ~ 8.0 Å (corresponding to the long molecular axis) (*31*), indicating that the long axis of the TFSI anion almost fully contributes to the lattice expansion, presumably by taking an end-to-end configuration with the alkyl side chain of PBTTT, as schematically illustrated in Fig. 2F.

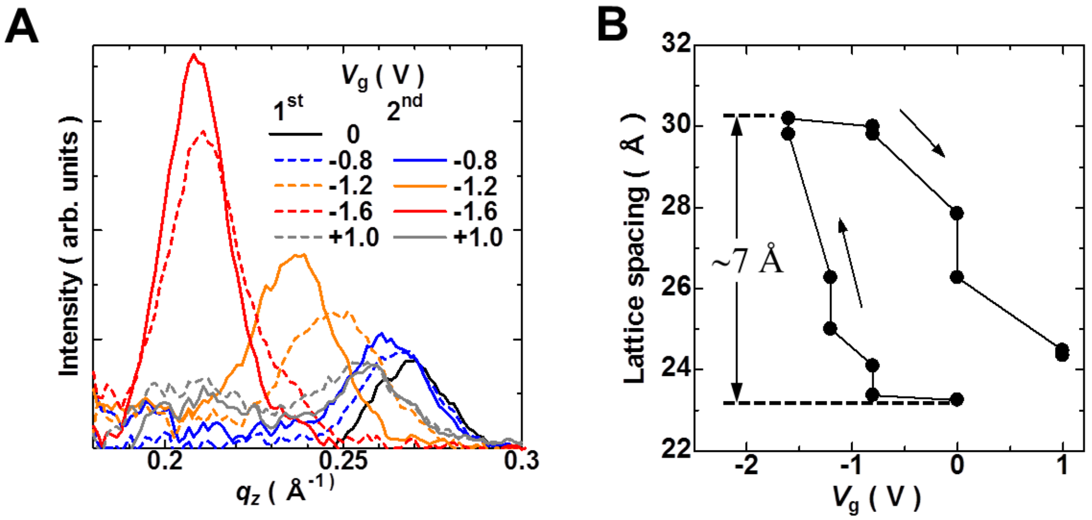

Fig. S2. In situ GIXD measurements of electrolyte-gated PBTTT thin films. (**A**) The V_g dependence of the out-of-plane (100) peak and (**B**) corresponding lattice spacing. The two data obtained with the same V_g values in A correspond to the results of the first and second measurements performed with 20 minutes' interval at each V_g value obtained during the upward $|V_g|$ scan. The arrows in B represent the scan direction of $|V_g|$.

Section S4. AFM imaging of the PBTTT thin film

In addition to the GIXD measurements, which demonstrate the high crystallinity of the PBTTT thin films, AFM imaging of the film surface easily visualizes the highly crystalline nature of the thin film (27, 54). Fig. S3 shows an AFM image of the PBTTT thin film fabricated on a glass substrate followed by annealing at 180 °C. We observe a clear terrace structure with a typical domain size on the order of ~100 nm, showing a molecularly flat surface and molecular steps, as reported in the literature (*27, 54*). The large crystalline domain size with a small portion of amorphous region is key to enhancing σ (or mobility) in the PBTTT thin film, whereas the domain boundaries are the dominant limiting factor of macroscopic charge transport.

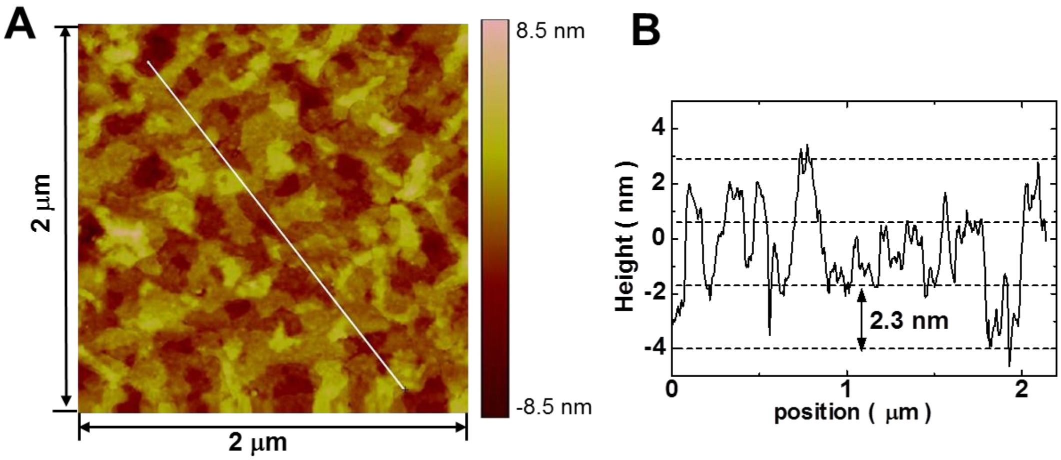

Fig. S3. AFM imaging of the PBTTT thin film. (**A**) A 2 mm × 2 mm AFM image of the PBTTT thin film on a glass substrate. (**B**) The height profile along the straight line in a). The horizontal dashed lines are drawn in every 2.3 nm separation, corresponding to the thickness of the monolayer, as determined by the GIXD measurements.

Section S5. Anisotropy of the ESR parameters

S5-I. Anisotropy of the *g* value and hyperfine interaction in the lowly doped state

It has been well demonstrated that the anisotropy of the *g* value and hyperfine-determined ESR linewidth in lightly doped polymers provide crucial information about the local molecular orientation around the carriers in conducting polymers (*34, 55-57*). Fig. S4A shows the angular dependence of the *g* value, as determined from the resonance magnetic field ($g = h\nu/\mu_B H_0$, where h, ν, μ_B, and H_0 are Plank's constant, microwave frequency, Bohr magneton, and the resonance magnetic field), and the peak-to-peak linewidth (ΔH_{pp}) reported for the lightly doped PBTTT thin film by using the ionic-liquid-gated TFT structure (*33*). In the lightly doped state, the *g* value exhibits a maximum ($g_\perp \sim 2.003$) with an external magnetic field (**H**) perpendicular to the substrate, whereas the linewidth exhibits a minimum in the same direction. From the DFT calculations, the maximum *g* value is expected to be along the short molecular axis (x axis, shown in Fig. S4B) with the principal value of $g_x = 2.0027$ (*34*), which is close to the $g_{\perp}$ value observed in Fig. 3B and Fig. S4A. This result indicates that the short molecular axis points substrate normal, which indicates the edge-on orientation. The anisotropy of the linewidth reflects the anisotropy of the proton hyperfine interaction, the maximum value of which tends to be observed along the chain axis (y-axis in Fig. S4B) and the minimum value of which is observed along the x-axis in thiophene-based polymers (*55*, *56*). Thus, this anisotropy explains the angular dependence of ΔH_{pp} in Fig. S4A by assuming the edge-on orientation.

Fig. S4C, D shows the angular dependence of the g value and linewidth observed in the present study with higher doping levels ($\sigma > 1$ S/cm) than in the case in Fig. S4A. The g value takes a maximum in the $H_{\perp}$ configuration independent of the conductivity (or doping level) with $g_{\perp} \sim 2.003$, indicating that the edge-on orientation is maintained even in the highly doped states, consistent with the GIXD experimental results in Fig. 2 and Fig. S2. In contrast, the linewidth exhibits completely different angular dependence from that in the lowly doped state shown in Fig. S4A, as discussed below.

S5-II. Anisotropy of the ESR linewidth in highly doped states

In the highly doped states shown in Fig. S4C, D, the ESR linewidth becomes much broader than that in the lightly doped state in all the magnetic field configurations. In addition, we observe a clear change in the angular dependence from that in the lightly doped state; i.e., both the g value and the linewidth exhibit the maximum at $\theta = 0°$. This anisotropy change indicates qualitative modification of the spin dynamics upon doping. The positive correlation between the g value and the linewidth is indicative of the Elliott mechanism, where the shortening of the spin-lattice relaxation time due to the spin-flip scattering of conduction electrons by phonons determines the linewidth (*36*), Since the spin-phonon interaction is mediated by the spin-orbit interaction, as in the case of the *g*-shift from the free electron *g* value (2.0023), the *g* value and the linewidth in this case correlate with each other. Indeed, a highly correlated angular dependence of these two parameters has been observed in several organic conductors (*58, 59*). Thus, the anisotropy change in ΔH_{pp} upon carrier doping in Fig. S4C, D is reasonably ascribed to the Elliott mechanism, indicating the delocalization of charge carriers in the high-conductivity region (σ_{RT} > 1S/cm).

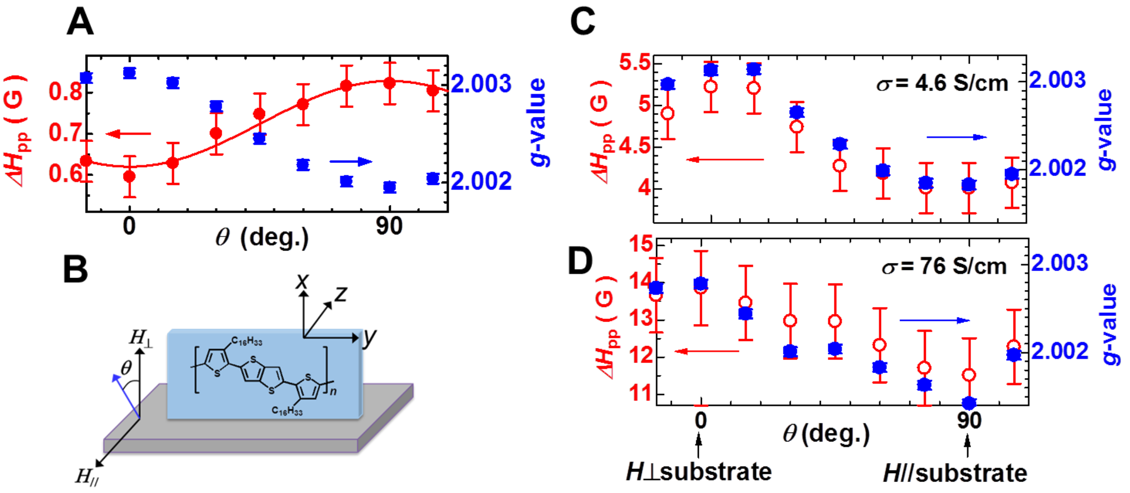

Fig. S4. Angular dependence of the ESR parameters at various doping levels. (**A**) The angular dependence of the *g* value and linewidth (ΔH_{pp}) reported for a lowly doped state using the electrolyte-gating technique (data taken from ref. *31*). (**B**) Schematic illustration of the magnetic field configurations and the principal axes of the *g* tensor. (**C**), (**D**) The angular dependence of the *g* value and ΔH_{pp} obtained at different conductivities, respectively, where the line broadening in Fig. 3E is observed.

Section S6. DFT calculation of backbone rigidity in the neutral and cationic states

The molecular backbone of PBTTT can be planarized by carrier doping, as demonstrated by the structural optimization by DFT calculations shown in Fig. 5C. Here, we further consider the structural resilience of the neutral and cationic states against torsional disorder. Fig. S5 shows the calculated torsion potentials of the neutral (blue triangles) and cationic (red circles) states with respect to the dihedral angles between the thiophene-thiophene (T-T) subunits (A) and the thienothiophene-thiophene (TT-T) subunits (B). It is immediately recognized that the cationic state exhibits a much higher potential increase against the torsion from the optimized structure than the neutral state for both T-T and TT-T bonds, although the TT-T bonds are more susceptible to the torsional disorder than the T-T bonds, as in the case of the neutral state. In the optimized structure of the neutral state, the TT-T unit shows a torsion angle of ~40 degrees from the planar conformation (180 degrees). However, this conformation becomes energetically destabilized in the cationic state as the energy increases as high as ~80 meV from the optimized structure in the present calculation, which presumably causes reorganization of the backbone to the planar structure dynamically after doping. The larger energetic slope in the cationic state, as described above, indicates that the doped PBTTT is more resilient to the torsional disorder induced by, for example, thermal fluctuations and interactions with dopant anions, acting as better tie molecules connecting the adjacent crystalline domains.

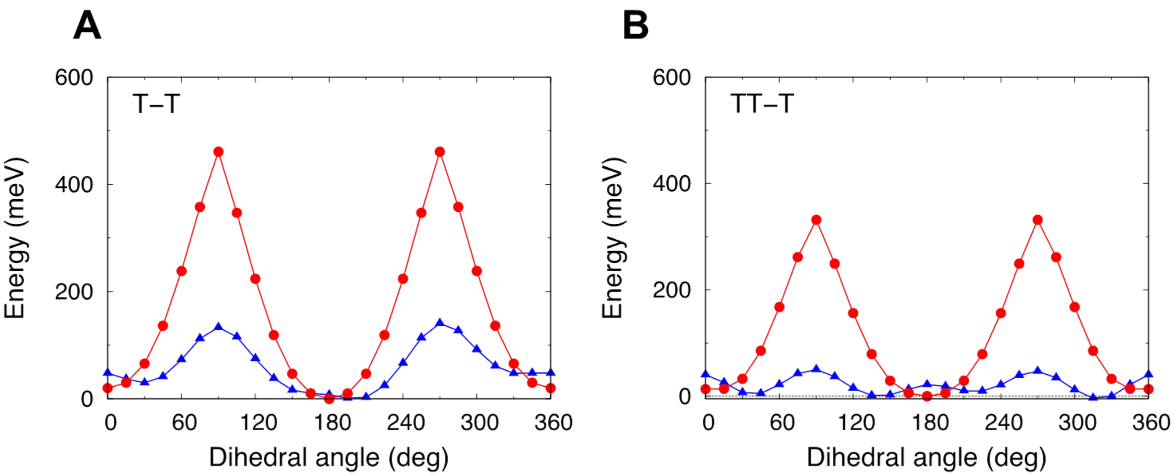

Fig. S5. DFT calculation of the torsion potential. (**A**) Torsion potentials calculated for thiophene-thiophene (T-T) subunits and (**B**) thienothiophene-thiophene (TT-T) subunits by the DFT method. The blue triangles show the results for the neutral state, and the red circles show those for the cationic state.